Present Status of Rare-earth Free Ferrimagnet Mn₄N and Future Prospects of Mn₄N-based Compensated Ferrimagnets

Takashi Suemasu[1], Laurent Vila[2], and Jean-Philippe Attané[2]

[1]*Department of Applied Physics, Faculty of Pure and Applied Sciences, University of Tsukuba,
Tsukuba, Ibaraki 305-8573, Japan*
[2]*Spintec, CNRS, CEA, Université Grenoble Alpes, 38054 Grenoble, France*

The rare-earth-free ferrimagnet Mn_4N has attractive features for spintronics applications, because it possesses a perpendicular magnetization, due to a relatively large magnetic anisotropy constant of $\sim 10^5 \, J \, m^{-3}$ and a small spontaneous magnetization of $\sim 100 \, kA \, m^{-1}$, and a large spin polarization ($P = 0.8$). More crucially, it is possible to reach the magnetic compensation at room temperature, by tuning its constituent elements in compounds such as $Mn_{4-x}Ni_xN$ and $Mn_{4-x}Co_xN$. This is particularly interesting for spin-torque-based spintronics applications, because at the vicinity of the magnetization and/or angular momentum compensation points, the switching currents can be reduced significantly, thereby leading to lower switching energies and higher switching speed. In this review article, we emphasize the importance of epitaxial growth of Mn_4N films by comparing the results obtained on two different substrates, MgO(001) and SrTiO₃(001). We then present the achievement of ultrafast current-induced domain wall motion (CIDWM) in Mn_4N microstrips, and study the magnetic compensations in $Mn_{4-x}Ni_xN$ and $Mn_{4-x}Co_xN$ at room temperature, proved by x-ray magnetic circular dichroism measurements. Finally, we offer future prospects for such Mn_4N-based compensated ferrimagnets.

1. Introduction

The ability of spin-transfer torques (STTs) and spin–orbit torques (SOTs) to induce magnetization precession and switching is the basis of a whole range of existing or emerging spintronics technologies.[1] In this context, ferrimagnets (FIM) have attracted an increasing attention.[2–15] Their key feature is that their spontaneous magnetizations are much smaller than those of ferromagnets, because the magnetic moments of different sublattices are aligned antiparallel to each other. This parameter is an important asset to develop applications based on STTs and SOTs, in which a flux of angular momentum carried by an incoming spin polarized current acts on the magnetization, inducing magnetization precession and/or switching. In the case of STTs, the spin polarized current is generated within a magnetic layer by the exchange interaction. In the case of SOTs, a pure spin current (i.e., a flow of angular momentum without net charge current) can be generated by spin Hall effect, frequently within a heavy metal layer in contact with the magnetic layer. It can also be produced by the Rashba Edelstein effect, at interfaces breaking the inversion symmetry, or in topological insulators. In all cases, the torque is due to the conservation of angular momentum. When the ferrimagnet is at the vicinity of the magnetic compensation (MC) (and/or angular momentum compensation), the incoming flow of angular momentum affects easily the reduced magnetization, and thus the critical current density necessary for magnetization switching decreases.[5,7,16] Ferrimagnets are thus appealing materials to develop STTs and SOTs-based devices such as domain wall memories, skyrmion-motion-based devices, three terminal magnetic random-access memories, SOT oscillators,[17] and others.[18,19] The most common route used in spintronics to achieve MC is based on alloys combining rare-earth elements and transition metals such as $Gd_{0.44}Co_{0.56}$ and $Tb_{0.21}Co_{0.79}$.[3,5,6,12,13] When the magnetization of the two species aligns antiparallel, there exists a single concentration at which the compensation
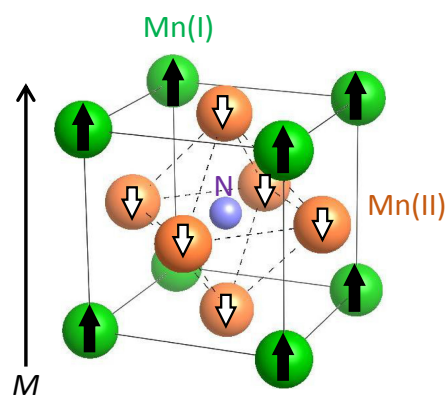

Fig. 1. (Color online) Anti-perovskite-type crystal structure of Mn₄N. The magnetic moment of the corner-site Mn atoms, Mn(I), is antiparallel to that of the face-centered Mn atoms, Mn(II), and parallel to the overall magnetization (black arrows).

occurs at room temperature (RT). Here, we have paid special attention to rare-earth free ferrimagnets as they alleviate the need of critical elements for spintronics. In Mn₄N, MC can be reached at RT just by tuning its constituent elements in $Mn_{4-x}Ni_xN$ and $Mn_{4-x}Co_xN$ films.[20–23]

Anti-perovskite Mn₄N is ferrimagnetic, and has a Curie temperature of 740 K in bulk Mn₄N,[24] while Fe₄N, Co₄N, $Fe_{4-x}Co_xN$, and $Fe_{4-x}Ni_xN$ samples possessing the same structure are ferromagnetic[25–30] at RT. On the other hand, Ni₄N is paramagnetic at RT.[30,31] As shown in Fig. 1, there are two inequivalent Mn sites: those at the corner sites, Mn(I), and the others at the face-centered sites, Mn(II). N atoms are positioned at the body-centered sites. Neutron diffraction in bulk Mn₄N revealed that the magnetic moment of Mn(I) is $3.5 \, \mu_B$, while that of Mn(II) is $-0.8 \, \mu_B$ at 300 K,[32] where μ_B is the Bohr magneton. Thus, the magnetic moments of the Mn(I) atoms determine the direction of magnetization, which is consistent with experimental results obtained by x-ray magnetic circular dichroism.[22] Theoretical calculations

predict that the Mn(II) atoms can be divided further into A and B sites, and that the magnetic moments of Mn(II) atoms at A sites are aligned parallel to the magnetization,[22,33,34] while they are aligned antiparallel to those of the Mn(II) atoms at B sites and of the Mn(I) atoms. Such discrepancies between theory and experiment indicate the need for a more advanced theoretical modeling with the core hole-$3d$ and $3d$–$3d$ interactions. The electron state of Mn_4N has been studied extensively.[35–37] According to an electron diffraction study using 50-nm-thick polycrystalline Mn_4N films, the N atom in Mn_4N was found to behave as an electron acceptor, and the electron state of Mn_4N was expressed as $Mn^0(Mn^{+0.2})_3N^{-0.6}$.[36] This is different from the donor model applicable to ferromagnetic Fe_4N, wherein one electron is donated from the N atom to each of the three face-centered Fe atoms.[38]

The interest of this material for spintronics arises from several features.

i) The combination of a relatively large perpendicular magnetic anisotropy (PMA) with a small spontaneous magnetization (M_S) leads to perpendicular magnetization, i.e., to the appearance of an out-of-plane easy axis of magnetization. This perpendicular magnetization allows downscaling spintronic devices, and storing data permanently using a bistable magnetization state in STT and SOT-based applications. PMA has been reported in Mn_4N films deposited on various substrates, including glass, Si(001), MgO(001), $SrTiO_3$[STO](001), $(LaAlO_3)_{0.3}(Sr_2TaAlO_6)_{0.7}$[LSAT](001), and $LaAlO_3$-(001),[39–46] and the in-plane tensile strain has been proposed to be the origin of PMA.[42,46] In this context, Mn_4N thin films are interesting candidates as they have been reported to have a relatively small $M_S \sim 100$ kA/m,[32,44,47] with an anisotropy field value $\mu_0 H_K > 2.5$ T.[33,42] An interesting point is that Mn_4N films are under tensile stress even when grown on LSAT(001), which has a smaller lattice constant than Mn_4N, corresponding to a lattice mismatch of 0.8%[45] that might be considered to induce a compressive stress in Mn_4N layers. The uniaxial magnetic anisotropy constant (K_u) of Mn_4N thin films has been reported to be of the order of 10^5 J/m^3.[44,47–49] A theoretical study has been recently conducted on the contribution of N to the in-plane tensile strain and to the resultant PMA in Mn_4N.[34] Materials such as Mn_4N, where the PMA is large enough to overcome the demagnetizing field energy, are perpendicularly magnetized.

ii) The effective spin polarization extracted from domain wall (DW) velocity measurements in Mn_4N[16] is relatively high ($P = 0.8$). This allows enhancing the magnetotransport effects used in spintronics such as the Anomalous Hall effect or the giant magnetoresistance, and suggests for instance that Mn_4N could be used as a magnetic soft layer in a magnetic tunnel junction stack.

iii) The magnetization reversal occurs through nucleation and the motion of Bloch DWs. The combination of a relatively large spin polarization with a small M_S leads to high domain wall velocities due to the STT.[16] The current-induced velocity due to the adiabatic torque is indeed given by

$$v \approx \frac{1}{1 + \alpha^2} \frac{g\mu_B}{2eM_S} PJ \propto \frac{P}{M_S} \qquad (1)$$

where v is the DW velocity, α the damping constant, g the Landé factor, e the electron charge, and J the current density. Note that the interest of the small magnetization is not restricted to the case of pure STT on DWs: for both STT through magnetic tunnel junction and for SOTs, the torque efficiency is supposed to vary as the inverse of the free layer magnetization.

iv) The combination of a high PMA with a reasonable exchange constant leads to relatively sharp Bloch walls. Sharp DWs could lead to an enhanced spin transfer effect through the non-adiabatic contribution[50] and contribute to faster DW motion at smaller currents.[49] The width of the DW (Δ) in the nanowire is given by Eq. (2):[51]

$$\Delta = \sqrt{A/K_u} \qquad (2)$$

where A is the exchange stiffness. As K_u increases, Δ decreases, leading to the reduction in the threshold current density (j_{th}) necessary to move the DWs.[49,52] In this respect, materials with PMA are advantageous for current-induced domain wall motion (CIDWM) devices. Furthermore, the DW width needs to be small enough to scale DW-based logic devices,[53] and three terminal or racetrack memories[54] down to the ultimate technology nodes.

v) Mn_4N does not require chemical elements deemed as critical from geopolitical and environmental points of view, such as heavy metals and rare-earth.

In this review article, we begin by underlining the importance of a high-quality thin-film growth on the magnetic properties, by comparing the epitaxial growth of Mn_4N films on STO(001) and MgO(001) substrates.

2. Formation and Characterizations of Mn4N Films on STO(001) and MgO(001)

10-nm-thick Mn_4N layers were grown on MgO(001) and STO(001) substrates at 450 °C, using a molecular beam epitaxy system with an ion-pump (10^{-7} Pa), equipped with a high temperature Knudsen cell for Mn and a radio-frequency (RF) N_2 plasma.[33,42] To prevent oxidation, the samples were capped with 3-nm-thick SiO_2 layers. In the case of STO(001) substrates, we used a buffered NH_4F-HF solution with controlled pH values to obtain TiO_2 atomic plane-terminated surfaces, with steps one unit cell in height.[55] The crystalline quality of the Mn_4N layers was characterized by 20-kV reflection high-energy electron diffraction (RHEED), and X-ray diffraction (XRD) with a Cu Kα radiation source. Magneto-transport properties, such as the magnon-magneto-resistance (MMR)[56,57] and the anomalous Hall effect (AHE), were measured by the Van der Pauw method for Mn_4N blanket layers at RT.[58] The transverse voltage (V_y) can be expressed as Eq. (1):[59]

$$V_y = \left(R_H \frac{B_Z}{t} + \frac{\rho_{AHE}}{t} \right) I_x = \frac{\rho_{xy}}{t} I_x, \qquad (1)$$

where R_H, B_Z, t, ρ_{AHE}, I_x, and ρ_{xy} are the normal Hall coefficient, the magnetic flux density perpendicular to the sample surface, the film thickness, the anomalous Hall
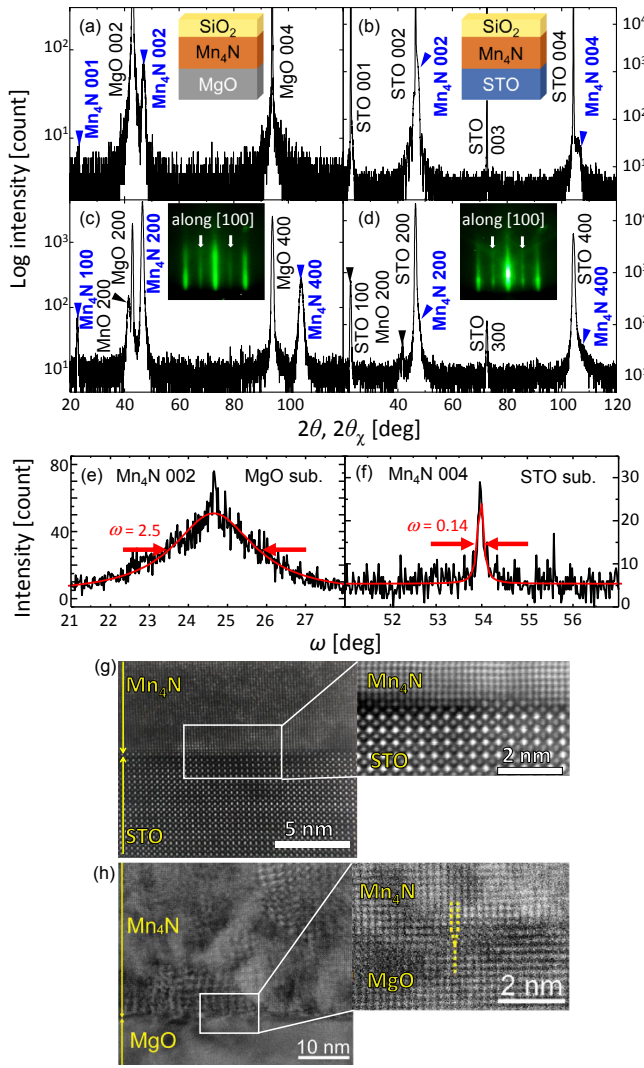
Fig. 2. (Color online) XRD profiles of Mn$_4$N films on (a, c, e) MgO(001) and (b, d, f) STO(001) substrates. Reproduced from Ref. 58 (©2018 Japan Society of Applied Physics) (a, b) Out-of-plane XRD patterns. The insets show the stack structures. (c, d) In-plane XRD patterns. The incident angle is $\omega = 0.4°$, and the scattering vector is along the [100] of Mn$_4$N films. The insets show the RHEED images of the Mn$_4$N layers along the [100] direction of each substrate. Arrows indicate the superlattice diffractions from N atoms at the body-centered site. (e, f) ω-scan rocking curves for Mn$_4$N films on MgO(001) and STO(001), respectively. TEM cross sections of Mn$_4$N films on (g) STO(001), reproduced from Ref. 16 (©2019 American Chemical Society), and (h) MgO(001), reproduced from Ref. 43 (©2014 AIP Publishing).

resistivity, the longitudinal current, and the Hall resistivity, respectively.

Figures 2(a) and 2(b) show out-of-plane XRD profiles of Mn$_4$N epitaxial films on MgO(001) and STO(001) substrates, respectively.[58] Figures 2(c) and 2(d) are their in-plane XRD profiles when the scattering vector was set to be along [100]. In both samples, oriented diffraction peaks such as 002 and 004 together with RHEED streaks are the proof of the epitaxial growth of Mn$_4$N films. Superlattice diffractions from N atoms positioned at the body-centered site, marked by arrows, are also present. However, there is a big difference in crystalline quality between them. ω-scan rocking curves are shown in the same figure for (e) Mn$_4$N 002 and (f) Mn$_4$N 004. We used the higher-order Mn$_4$N 004 for Mn$_4$N films on STO because the peak position of Mn$_4$N 002 is close to STO
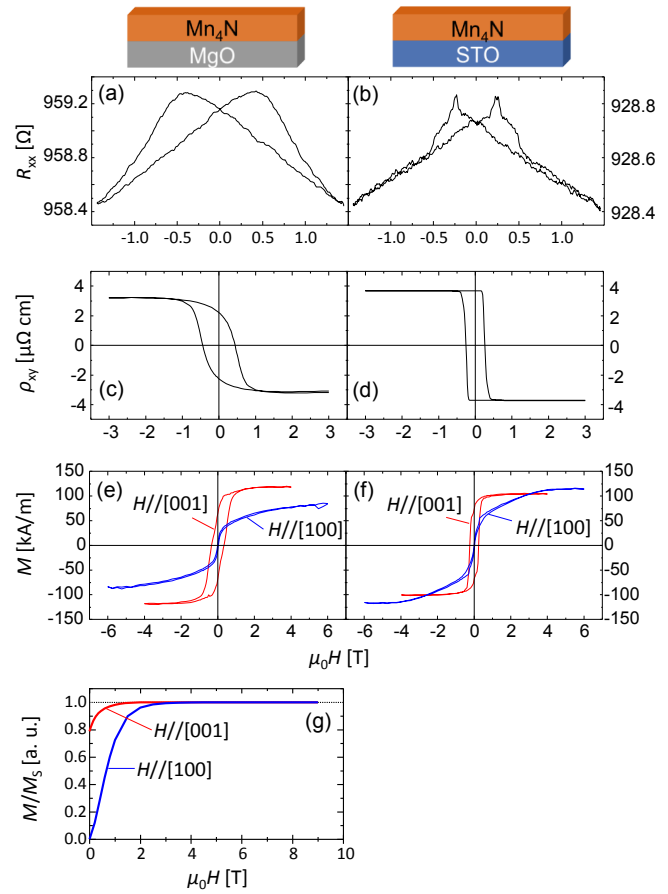

Fig. 3. (Color online) (a, b) Longitudinal resistance against magnetic field normal to the plane, (c, d) Anomalous Hall effect hysteresis loops, and (e, f) Out-of-plane hysteresis loops measured by VSM. Reproduced from Ref. 58 (©2018 Japan Society of Applied Physics). (a, c, e) correspond to the Mn$_4$N films on MgO(001), and (b, d, f) to the Mn$_4$N films on STO(001). (g) Normalized out-of-plane and in-plane components of the magnetization obtained from AHE measurements on the Mn$_4$N films on MgO(001).

002 in Fig. 2(b). According to the fitting by a Lorentzian function, the full-width at half maximum was 2.5 and 0.14 deg for Mn$_4$N films on MgO and STO, respectively. The lattice constant of MgO is 0.421 nm, and that of STO is 0.391 nm. Thereby, the lattice mismatch for Mn$_4$N/MgO(001) and Mn$_4$N/STO(001) are approximately -7.6 and -0.4%, respectively, assuming that the Mn$_4$N films has a cubic structure and a lattice constant of 0.389 nm.[32] Such a small lattice mismatch between Mn$_4$N and STO leads to the perfect epitaxial growth of Mn$_4$N/STO[16] as shown in Fig. 2(g), whereas misfit dislocations are observed for Mn$_4$N/MgO[43] in Fig. 2(h).

Figures 3(a) and 3(b) show the dependence of the longitudinal resistance R_{xx} with the magnetic field normal to the sample surface. The resistivity ρ_{xx} is 187 $\mu\Omega$ cm for the Mn$_4$N/MgO sample, and 181 $\mu\Omega$ cm for the Mn$_4$N/STO sample at RT. As shown in these figures, the magnetoresistance is dominated by the magnon magnetoresistance, typically observed in samples with a strong uniaxial anisotropy.[60] Figures 3(c) and 3(d) show the hysteresis loops measured by AHE. The AHE angle ρ_{xy}/ρ_{xx} is high (-2%), in line with previous reports on Mn$_4$N.[61,62] The coercivity of the Mn$_4$N/STO sample (0.26 T) is slightly smaller than that of the Mn$_4$N/MgO sample (0.44 T). These relatively high coercive fields are due to the small saturation

magnetization. The Mn$_4$N/MgO sample shows a smooth hysteresis loop. In contrast, the magnetization of the Mn$_4$N/STO sample switches very sharply, with a full remanence at zero field. Despite these differences, it is striking that the spontaneous magnetization and all the transport quantities of the two systems are very similar. This result indicates that the Mn$_4$N films in the two samples are intrinsically alike, regardless of the different substrates and thus of different lattice mismatches. The increased disorder in the Mn$_4$N films on MgO widens the nucleation and DW pinning field distribution associated to the defects, thus leading to a higher coercivity and a slanted hysteresis loop. Figures 3(e) and 3(f) present the hysteresis loops for in-plane and out-of-plane fields, obtained by VSM-SQUID up to 4 and 6 T, respectively. From the out-of-plane hysteresis curves, the M_S of Mn$_4$N/MgO and Mn$_4$N/STO samples was found to be 118 and 105 kA m^{-1}, respectively. From the in-plane loop of Mn$_4$N/STO, the anisotropy field $\mu_0 H_K$ was estimated to be 4.0 T. The uniaxial anisotropy K_u was calculated to be 1.1×10^5 J m^{-3}, using the integration of the area enclosed between the in-plane and out-of-plane magnetization curves, and taking into account the demagnetization energy. On the other hand, the area is not enclosed for the Mn$_4$N/MgO sample in Fig. 3(e). This is because the sensitivity of the VSM-SQUID setup was not good enough to precisely measure the saturation field, for subtracting the contribution of the MgO substrate (especially in the in-plane H configuration). Figure 3(g) shows the normalized out-of-plane and in-plane components of magnetization obtained from AHE measurements on the Mn$_4$N films on MgO(001). K_u and $\mu_0 H_K$ were calculated to be 6.1×10^4 J/m^3 and 1.3 T, respectively. We attribute the difference in these values between Mn$_4$N/STO and Mn$_4$N/MgO samples to the crystalline inhomogeneity caused by defects in the Mn$_4$N/MgO sample as shown in Fig. 2. Now we can discuss the magnetic domain configuration in Mn$_4$N thin films on STO. The theoretical equilibrium domain size in Mn$_4$N layers is determined by the balance between the dipolar energy and the DW energy. From the measured values of $M_S = 105$ kA m^{-1}, $K_u = 1.1 \times 10^5$ J m^{-3}, and $A = 15$ pJ m^{-1} (using a rough estimation from the Curie temperature),[63] the DW width can be calculated to be $\Delta = \sqrt{A/K_u} = 11$ nm. The resulting equilibrium domain size for a 10-nm-thick Mn$_4$N film, calculated using the analytical model of Ref. 64, is of several km. This indicates that the demagnetizing field is negligible because of the small M_S, and that in practice the domain size and shape are rather determined by DW pinning on extrinsic defects.[65] Hereafter, we focus on Mn$_4$N epitaxial films on STO(001).

Let us examine the domain pattern in Mn$_4$N layers on STO substrates. The magnetic domain configuration was observed by magneto-optical Kerr effect (MOKE) microscopy. The observation was performed both for the as-deposited state in Fig. 4(a) and for a partially reversed state in Fig. 4(b), corresponding to the red dot state in the magnetization curve shown in Fig. 4(c). In Fig. 4(a), the magnetic domain size d_p is as large as 20 μm, with smooth magnetic DWs. This value is comparable with the equilibrium value of ultrathin CoFeB (1.1 nm)/MgO(1) and Pt(2.4)/Co(0.27) system, with d_p values of respectively 14 and 6.5 μm obtained after thermal demagnetization.[66,67] Figure 4(b) presents the domain con-
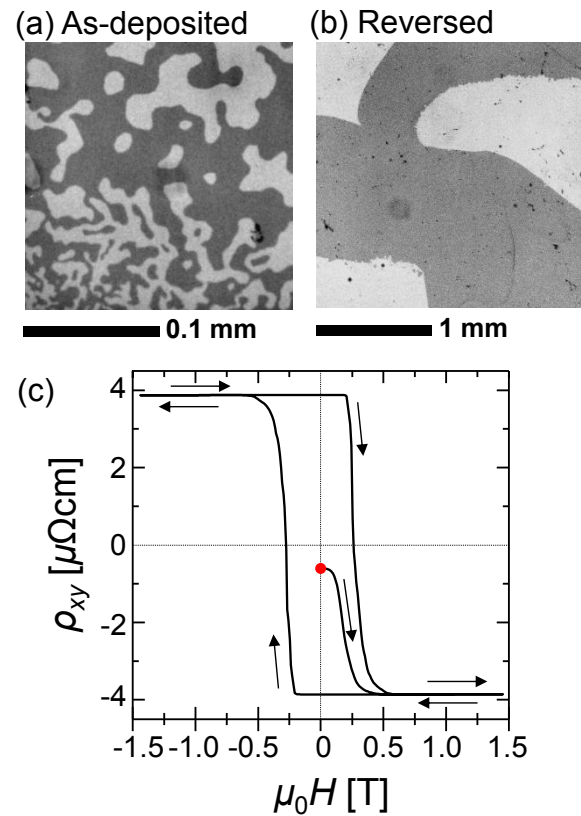

Fig. 4. (Color online) (a) MOKE image of the Mn$_4$N films on STO(001) in the as-deposited state, (b) MOKE image of the sample after the partial reversal of (c), and (c) magnetization curve illustrating the partial reversal process, monitored by anomalous Hall effect in the sample. Reproduced from Ref. 58 (©2018 Japan Society of Applied Physics). The red dot corresponds to the final magnetization state, used for (b).

figurations in partially reversed states. The domain size in Mn$_4$N/STO reaches a value as large as one millimeter. MOKE images show the presence of very few nucleation centers, showing that the magnetization switching occurs by nucleation, followed by an easy propagation of DWs. This observation is consistent with the fact that the hysteresis loop is square. Note that the use of MgO substrate leads to much smaller sub-micrometric domains, which is consistent with the observation of a larger disorder using structural and magnetic characterizations.[58] On the basis of these results, we can state that the selection of a well-matching substrate is crucial to improve the magnetic properties of Mn$_4$N layers, and notably its suitability for current-induced DW propagation.

3. Evaluation of DW Speed and Spin Transfer Efficiency

10-nm-thick Mn$_4$N epitaxial films were processed by ion milling into sets of twenty 1 or 2 μm wide microstrips, connected to two electric pads. The current flows through the microstrips in order to induce DW motion. After saturation of the magnetization, magnetic field pulses were applied to nucleate a domain in a pad and to inject DWs into the microstrips. The current pulses pushed the DWs. The DW displacement during the current pulses was measured using a differential MOKE imaging technique, consisting in subtracting the MOKE image before pulse injection from the image obtained after the pulse injection. This is to highlight
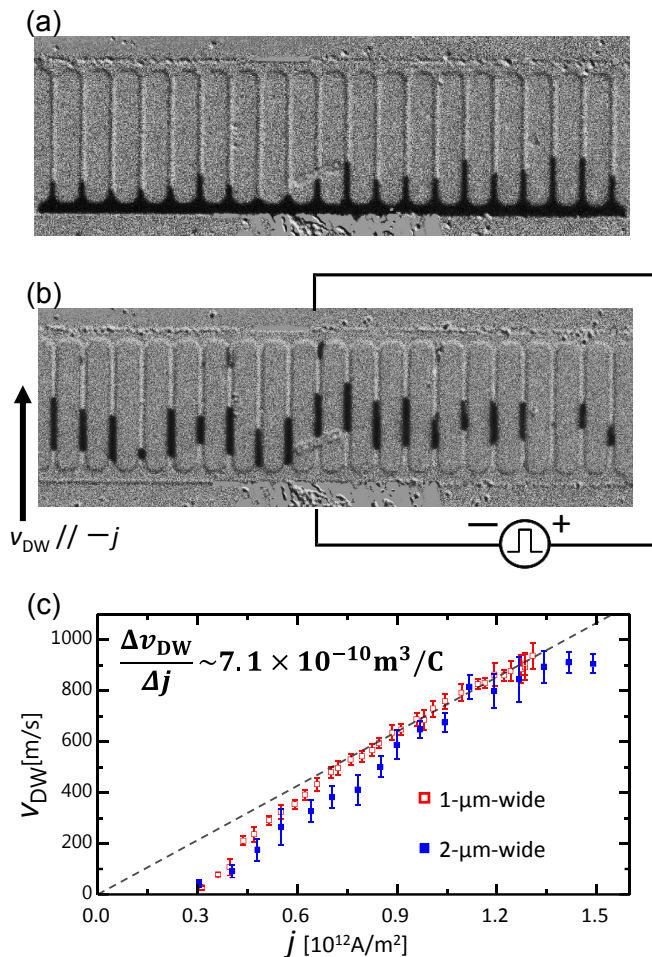
Fig. 5. (Color online) (a) Differential MOKE image after domain nucleation using a field pulse of 0.6 T. (b) Differential MOKE image after several 1 ns current pulses. The area through which the DW propagated appears in black. The DW motion direction is opposite to the current, and thus follows the electrons flow. (c) Current density dependence of v_{DW} measured at RT. Both the 1- and 2-μm-wide strips possess similar behaviors. The DW mobility is calculated to be $7.1 \times 10^{-10}\,\mathrm{m^3\,C^{-1}}$. Reproduced from Ref. 16 (©2019 American Chemical Society).

the difference between them and to show the corresponding magnetization reversal by DW displacement. Figure 5(a) shows the differential MOKE image after domain nucleation using a field pulse of 0.6 T for 300 μs, and Fig. 5(b) shows the differential MOKE image taken after injection of several 1 ns current pulses. The area through which the DW propagated appears in black. The DW motion direction is opposite to the current, and thus follows the electrons flow. Figure 5(c) presents the current density dependence of the DW velocity v_{DW}. The threshold current density for 1-ns-width pulse is $3.0 \times 10^{11}\,\mathrm{A\,m^{-2}}$. Above $8 \times 10^{11}\,\mathrm{A\,m^{-2}}$ in 1-μm-wide strips, the trend of the v_{DW} versus j curve becomes linear. In the studied range of current densities, the DW reached an average velocity of $900\,\mathrm{m\,s^{-1}}$, for a current density of $1.3 \times 10^{12}\,\mathrm{A\,m^{-2}}$ in both 1-μm and 2-μm-wide strips. This value is the highest in all materials and structures whose DW was driven by only pure STTs. The velocities observed in Mn$_4$N can thus be considered as a milestone in the history of STTs.

The large v_{DW} obtained in Mn$_4$N show that the STTs can be competitive with SOTs even though SOTs-driven DW

dynamics have been the focus of nearly the entire community in recent years. SOTs have indeed been found to be an efficient mechanism to drive DWs in non-centrosymmetric multilayers, in which a FM is deposited on a heavy metal like Pt.[68,69] The prototypical example is AlO$_x$/Co(0.6 nm)/Pt,[70] where the chiral Néel structure acquired by the DWs in the presence of interfacial Dzyaloshinskii–Moriya interaction (DMI)[71] leads to a high mobility ($v_{DW} = 400\,\mathrm{m\,s^{-1}}$ for $j = 3 \times 10^{12}\,\mathrm{A\,m^{-2}}$). Higher SOT-driven v_{DW}'s were obtained recently in a multilayer structure in which two Co/Ni layers were coupled anti-ferromagnetically through a Ru layer,[11] or in GdCo ferrimagnet layers deposited on top of Pt.[72] In these systems the v_{DW} was clearly observed to vary with the total magnetization. In the former experiment, a maximum velocity of $v_{DW} = 750\,\mathrm{m\,s^{-1}}$ for $j = 3 \times 10^{12}\,\mathrm{A\,m^{-2}}$ was obtained at RT using a Ru spacer layer. Thus, the stack magnetization was reduced to 8% of the M_S of a single Co/Ni layer. In the latter one, a peak velocity of $1300\,\mathrm{m\,s^{-1}}$ was reported at the compensation temperature, for $j = 2 \times 10^{12}\,\mathrm{A\,m^{-2}}$ and still high even at 300 K with $850\,\mathrm{m\,s^{-1}}$. Recently, SOT driven DW motion in insulating ferrimagnetic garnets have also led to similar DW speeds.[73] In this context, the v_{DW} presented here at RT for DWs in Mn$_4$N is comparable to the best results obtained using SOTs. Moreover, this constitute the first demonstration of very efficient current-driven DW motion by pure STT using a system with PMA. Another figure of merit of the STT efficiency is the DW mobility $\eta = \Delta v_{DW}/\Delta j$, that can be derived from the v_{DW} versus j curve, and is equal to $\eta = 7.1 \times 10^{-10}\,\mathrm{m^3\,C^{-1}}$. This mobility is also the highest value in all STT-driven systems, and is superior to most SOT-driven records. Above $1.3 \times 10^{12}\,\mathrm{A\,m^{-2}}$, many domains nucleate, probably because the sample reaches 745 K, the Curie temperature of Mn$_4$N, and becomes temporarily paramagnetic.

4. Formation and Characterizations of 3d-doped Compensated Mn$_4$N Films

On the basis of the DW experiments presented above, much faster v_{DW} can therefore be expected in the vicinity of the angular momentum compensation point, which is supposed to be close to the MC point in 3d-element-doped Mn$_4$N. In the past, Mekata et al. attempted to replace some of the Mn atoms in Mn$_4$N by In and Sn, and obtained the MC with appropriate composition ratios and temperature.[74] Here we present our recent results obtained on Mn$_{4-x}$Ni$_x$N and Mn$_{4-x}$Co$_x$N epitaxial films grown on STO(001). Preparation details are given in Refs. 21 and 23. We performed x-ray absorption spectroscopy (XAS) and x-ray magnetic circular dichroism (XMCD) measurements at the twin APPLE-II undulator beam line BL16A of KEK in Japan, to find a Ni ratio in Mn$_{4-x}$Ni$_x$N and a Co ratio in Mn$_{4-x}$Co$_x$N where the MC occurs at RT. These techniques are quite powerful to determine element-specific electronic structures. Among samples, Mn$_{4-x}$Co$_x$N ($x = 0.8$) was measured at the twin helical undulator beamline BL23SU of SPring-8 in Japan, wherein the measurements were performed using the total electron yield (TEY) mode both at the Mn $L_{2,3}$ and Co $L_{2,3}$ absorption edges.[22] All measurements were performed at RT. We also measured the AHE loops at RT for a magnetic field applied perpendicularly to the plane, using the Van der Pauw method.
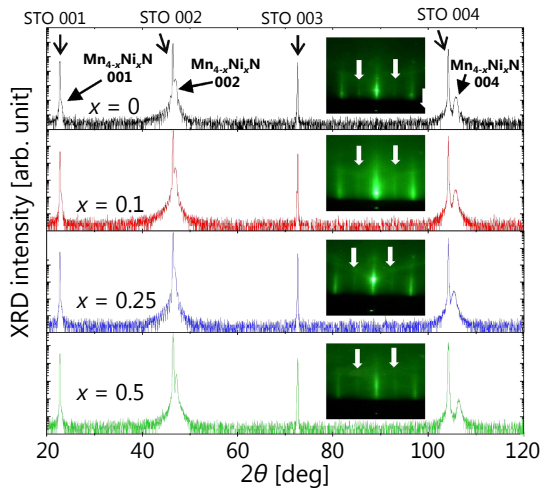
Fig. 6. (Color online) Out-of-plane XRD profiles of $Mn_{4-x}Ni_xN$ ($x = 0$, 0.1, 0.25, 0.5) films on STO(001). The insets show the RHEED patterns taken along the [100] azimuth. The arrows show superlattice diffractions from N atoms at the body-centered sites. Reproduced from Ref. 20 (©2019 AIP Publishing).

Fig. 7. (Color online) Dependence of the Hall resistivity ρ_{AHE} on a perpendicular magnetic field for $Mn_{4-x}Ni_xN$ ($x = 0, 0.1, 0.25, 0.5$) films on STO(001) at RT.

4.1 Mn substitution by Ni

We grew approximately 30-nm-thick $Mn_{4-x}Ni_xN$ ($x = 0$, 0.1, 0.25, and 0.5) thin films on STO(001) substrates at 450 °C by MBE, and covered the samples with an approximately 3-nm-thick capping layers. For this purpose, SiO_2 was used as capping layers for AHE measurements, while Ti was used for XAS and XMCD measurements. We independently controlled the deposition rates of Mn and Ni by changing the crucible temperature of each Knudsen cell. Figure 6 shows the out-of-plane XRD and RHEED patterns of the $Mn_{4-x}Ni_xN$ ($x = 0, 0.1, 0.25$, and 0.5) thin films along the STO[100] azimuth. Diffraction peaks of the grown layers appear at small 2θ angles in Fig. 6 and overlap with the intense diffraction peaks of the STO substrate. This is because of the excellent lattice match between the $Mn_{4-x}Ni_xN$ films and the STO(001) substrate. We see very sharp, streaky lines together with superlattice lines marked by arrows in the RHEED patterns, and Kikuchi lines verifying the highly c-axis-oriented epitaxial growth of the $Mn_{4-x}Ni_xN$ films. It is noted that the diffraction peaks of $Mn_{4-x}Ni_xN$ appear at slightly higher angles than those of cubic STO(001) in Fig. 6. This result indicates the presence of in-plane tensile strain in the $Mn_{4-x}Ni_xN$ films at $x \leq 0.5$.

Figure 7 shows the AHE loops for $Mn_{4-x}Ni_xN$ ($x = 0, 0.1$, 0.25, and 0.5) thin films at RT. It is noted that the sign of ρ_{AHE} was reversed for $Mn_{4-x}Ni_xN$ films between $x = 0.1$ and 0.25 in Fig. 7. This result indicates the crossing of the magnetic compensation point. Such a sign reversal is commonly used to confirm the presence of a MC point in rare-earth ferrimagnets.[4,5] The ratio of the remnant magnetization (M_r) to M_S, M_r/M_S, was almost 1 for $x = 0, 0.1$, and 0.25. In contrast, a much smoother magnetization reversal occurred in $Mn_{3.5}Ni_{0.5}N$ films, and a large magnetic field was required for their magnetization to saturate. The reasons for this behavior could be the degradation of the crystalline quality at $x = 0.5$ and the decrease of the magnetization, which can both contribute to an increase of the coercivity. We therefore chose the samples with $x = 0.1$ and 0.25, and performed XAS and XMCD measurements on them at RT.
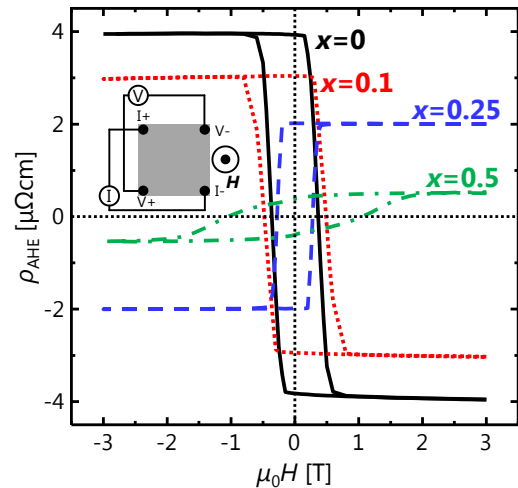
Figures 8(a) and 8(b) show the XAS (blue) and XMCD (black) spectra of $Mn_{3.9}Ni_{0.1}N$ and $Mn_{3.75}Ni_{0.25}N$ films at the Ni $L_{2,3}$ absorption edges, respectively. We applied both a magnetic field of ± 3 T and circularly polarized x-rays with left or right polarization perpendicularly to the plane. The x-ray polarization was switched at every energy point with a frequency of 10 Hz using five kicker magnets. We acquired spectra at the Mn $L_{2,3}$ absorption edges in the TEY mode, while those at the Ni $L_{2,3}$ absorption edges in the total fluorescence yield (TFY) mode. This prevents Ni $L_{2,3}$ spectra from overlapping with background signals. Regarding the XAS spectra of $Mn_{3.9}Ni_{0.1}N$ and $Mn_{3.75}Ni_{0.25}N$ films, we observe only the sharp main peaks at the L_3 edge (852–853 eV) and the L_2 edge (870 eV). Similar peaks were reported for $NiFe_3N$.[75] In contrast, shoulders appear in the XAS spectrum of Ni-rich Ni_3FeN films,[75] wherein Ni atoms unavoidably occupy face-centered II sites. We see these shoulders approximately 2 eV above the Ni $L_{2,3}$ main peaks. Such shoulders are reported also for other antiperovskite ferromagnetic nitrides such as Fe_4N and Co_4N films above the Fe (Co) $L_{2,3}$ main peaks.[76,77] They are interpreted to originate from the electric dipole transition from the metal $2p$ core level to the hybrid state between the orbitals of the N $2p$ and metal $3d$ at II sites, indicating that the objective element is at the face-centered sites in Fig. 1.[76] On the basis of these results, it can at least be stated that Ni atoms preferentially occupy the I sites in Mn_4N when $x \leq 0.25$. It is noted that the peak sign of the XMCD spectra at the $L_{2,3}$ edges are opposite between $Mn_{3.9}Ni_{0.1}N$ and $Mn_{3.75}Ni_{0.25}N$. This result means that the directions of the magnetic moments of Ni(I) in $Mn_{3.9}Ni_{0.1}N$ films are different from that in $Mn_{3.75}Ni_{0.25}N$ films with respect to magnetizations.

We next discuss the XAS (blue) and XMCD (black) spectra of $Mn_{3.9}Ni_{0.1}N$ and $Mn_{3.75}Ni_{0.25}N$ films at the Mn $L_{2,3}$ absorption edges in Figs. 8(c) and 8(d). Here we focus on the XMCD spectra. In $Mn_{3.9}Ni_{0.1}N$ films, the signs of the XMCD signals around the Mn L_3 edge are positive, negative, and positive from low to high photon energy as shown in Fig. 8(c). Such complex signals are caused by the superposition of spectra with different signs. This means that
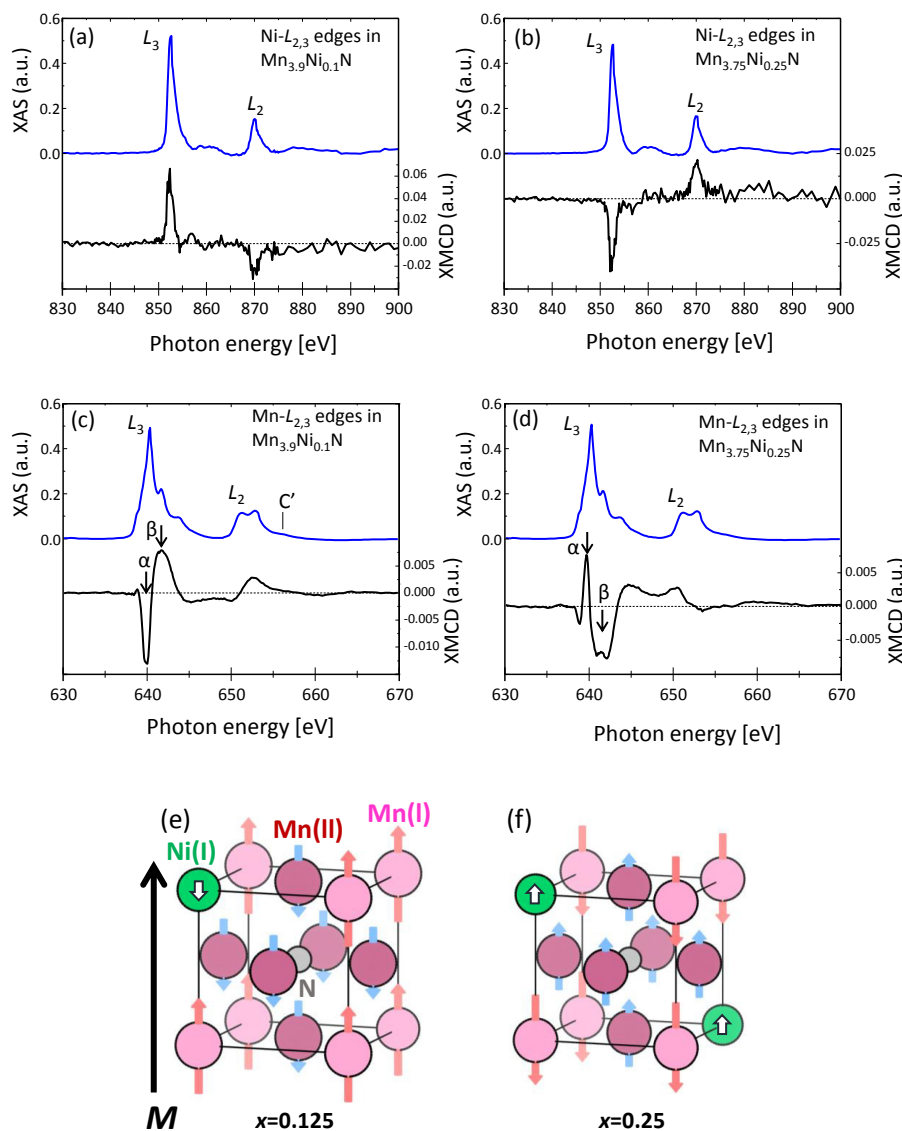
Fig. 8. (Color online) XAS (blue) and XMCD (black) spectra in (a, c) $Mn_{3.9}Ni_{0.1}N$ films and (b, d) $Mn_{3.75}Ni_{0.25}N$ films at (a, b) Ni-$L_{2,3}$ edges and (c, d) Mn-$L_{2,3}$ edges. Reproduced from Ref. 21 (©2020 AIP Publishing). The sharp peak (α) and broad peak (β) in (c, d) originate mainly from Mn(I) and Mn(II), respectively. The reversal of the XMCD signals between (a) and (b) and between (c) and (d) means that the direction of magnetic moments of Mn and Ni is reversed between them.

the magnetic moments of Mn(I) and Mn(II) are aligned antiparallel to each other. According to our previous studies on Fe_4N films, the transition metals at the I(II) site exhibited localized (itinerant) states. This is supported by first-principles calculation using the all-electron full-potential linearized augmented-plane-wave (FLAPW) method and Fermi's golden rule with E1 transitions.[76] Similar results are also obtained for Mn_4N using FLAPW calculation.[22] Therefore, we interpret the XMCD spectra of $Mn_{3.9}Ni_{0.1}N$ and $Mn_{3.75}Ni_{0.25}N$ films as being due to an overlap of such localized and itinerant components with opposite signs characterized by features α and β, respectively. In $Mn_{3.9}Ni_{0.1}N$ films, the broad positive peak (β) near 642 eV likely originates from Mn(II) atoms, caused by the hybridization between Mn(II) $3d$ and N $2p$ orbitals. In contrast, we attribute the sharp negative peak (α) near 640 eV to Mn(I), which is remote from the body-centered N atom, and therefore entails less hybridization. On the other hand, the signs of the XMCD signals near the Mn L_3 absorption edges

in Fig. 8(d) are negative, positive, and negative from low to high photon energy in $Mn_{3.75}Ni_{0.25}N$. This is the opposite to the results obtained for the $Mn_{3.9}Ni_{0.1}N$ films. We attribute this to magnetization reversal at both I and II sites of Mn atoms. Such behavior of the spectra was reported in ferrimagnets at the vicinity of the compensation temperature.[78,79] It is also noted that the XMCD signal at the Ni L_3 absorption edge has the same sign of the broad peak (β) for the Mn L_3 edge at 642 eV regardless of x, while it has the opposite sign of the sharp peak (α) at 640 eV. Thus, the magnetic moments of Ni(I) align in parallel with those of Mn(II) in the studied range of Ni content x. From these discussions, we conclude that the Ni atoms preferentially occupy the I site in $Mn_{4-x}Ni_xN$ thin films, and that the magnetic moments of Ni atoms are parallel to those of Mn(II). The simplified schematics of the magnetic structures in $Mn_{4-x}Ni_xN$ below the MC composition ratio in Fig. 8(e) and above it in Fig. 8(f). Therefore, we can safely state that the MC occurs at a certain value x between 0.1 and 0.25 at
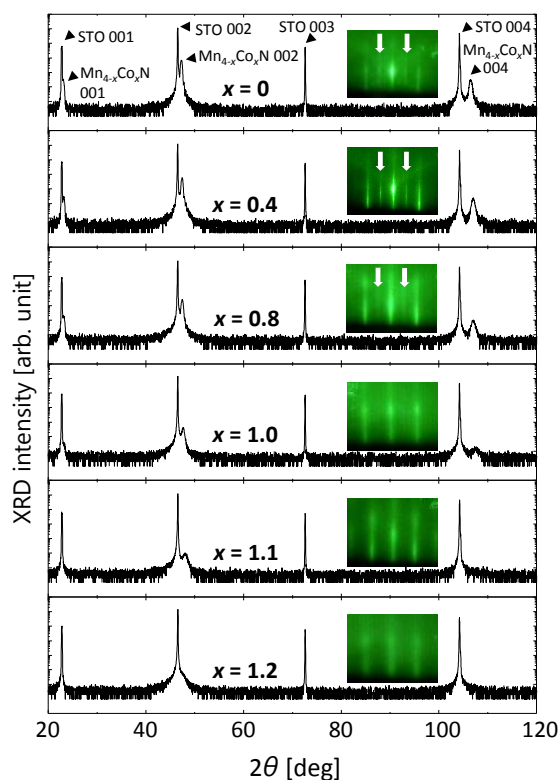
Fig. 9. (Color online) Out-of-plane XRD profiles of $Mn_{4-x}Co_xN$ ($x = 0$, 0.4, 0.8, 1.0, 1.1, 1.2) films on STO(001). The insets show the RHEED patterns taken along the [100] azimuth. The arrows indicate the superlattice diffractions from N atoms at the body-centered site. Reproduced from Ref. 23 (©2020 American Physical Society).

Fig. 10. Dependence of the anomalous Hall resistivity ρ_{AHE} on the perpendicular magnetic field for $Mn_{4-x}Co_xN$ ($x = 0, 0.2, 0.4, 0.6, 0.8, 1.0$, 1.1, 1.2) films on STO(001) at RT. Copyright 2020 American Physical Society. Reproduced from Ref. 23 (©2020 American Physical Society).

RT. In line with this experimental result, we recently achieved the extremely fast pure STT-driven v_{DW} exceeding $1,000\,m\,s^{-1}$ at RT at the vicinity of the MC in $Mn_{4-x}Ni_xN$ microstrips. The fastest one reached $3,000\,m\,s^{-1}$ at $x = 0.15$,[80] which exceeds three times the highest value ever reported ($v_{DW} = 900\,m\,s^{-1}$ in Mn_4N).[16] This result strongly suggests a pathway to attain an extremely high v_{DW}, that is to reduce M_S with keeping PMA in high-P materials.

4.2 Mn substitution by Co

We grew 30-nm-thick $Mn_{4-x}Co_xN$ ($x = 0$–1.3) thin films on STO(001) substrates at approximately $450\,°C$ by MBE with the deposition rates of Mn and Co independently controlled by the crucible temperature of each Knudsen cell. As approximately 3-nm-thick capping layers, we used SiO_2 for AHE measurements and Ta for XAS and XMCD measurements. Both a magnetic field of $\pm 5\,T$ and circularly polarized X-rays with left or right polarization were applied at an angle of $54.7°$ to the plane.[81] The X-ray polarization was switched at every energy point with a frequency of $10\,Hz$ using five kicker magnets. We adjusted the energy of the incident soft X-rays to include the L_2 and L_3 absorption edges of Mn and Co. The XAS spectra were obtained in TEY mode and TFY mode at the Mn $L_{2,3}$ and Co $L_{2,3}$ absorption edges, respectively.

Figure 9 shows the out-of-plane XRD profiles and RHEED patterns of the $Mn_{4-x}Co_xN$ thin films along the STO[100] azimuth. c-axis-oriented XRD peaks such as 001, 002, and 004 of $Mn_{4-x}Co_xN$ appeared at slightly higher angles compared to those of STO. For samples with
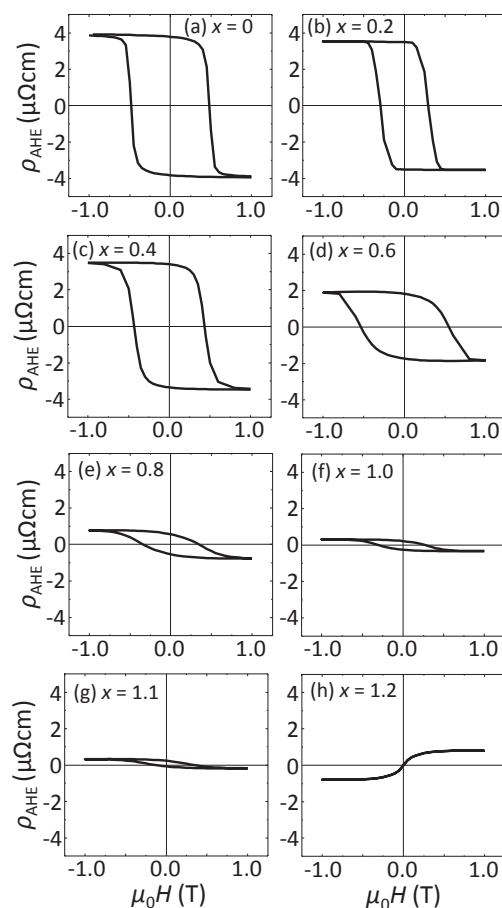
$x = 0$–1.1, we see the diffraction peaks of $Mn_{4-x}Co_xN$ 002 and 004 with RHEED streaks, showing the epitaxial growth of $Mn_{4-x}Co_xN$ films. We also confirm the superlattice diffractions indicated by the white arrows. They originate from N atoms at the body-centered site for samples with $x = 0$–0.8. With increasing x, however, the XRD peak intensity decreased, the RHEED streaks were blurred at $x = 1.2$, and the diffraction peak of 004 was not observed at $x = 1.1$ and 1.2. These results suggest that the crystalline quality degraded. The in-plane lattice constant a decreased from 0.389 to 0.384 nm when x increased from 0 to 1.3. The out-of-plane lattice constant c also decreased from 0.386 to 0.381 nm with keeping the in-plane tetragonal distortion ($c/a \sim 0.99$). Figures 10(a)–10(h) shows the ρ_{AHE} vs $\mu_0 H$ curves at RT. The magnitude of ρ_{AHE} decreases with x, and its sign reverses between $x = 1.1$ and 1.2. In the case of $Mn_{4-x}Ni_xN$ films, the sign reverses between $x = 0.1$ and 0.25 in Fig. 7, which is consistent with the MC composition for this material. We therefore chose the two samples ($x = 0.8$ and 1.3) together with one more sample ($x = 0.2$), and performed XAS and XMCD measurements at RT.

Figures 11(a)–11(c) show the XAS and XMCD spectra of $Mn_{4-x}Co_xN$ films ($x = 0.2, 0.8$, and 1.3) at the Co $L_{2,3}$ absorption edges, and Figs. 11(d)–11(f) show those at the Mn $L_{2,3}$ absorption edges, respectively. Here, we focus on the XMCD spectra. The peaks A and A′ in Figs. 11(a) and 11(b) have opposite signs. According to our previous
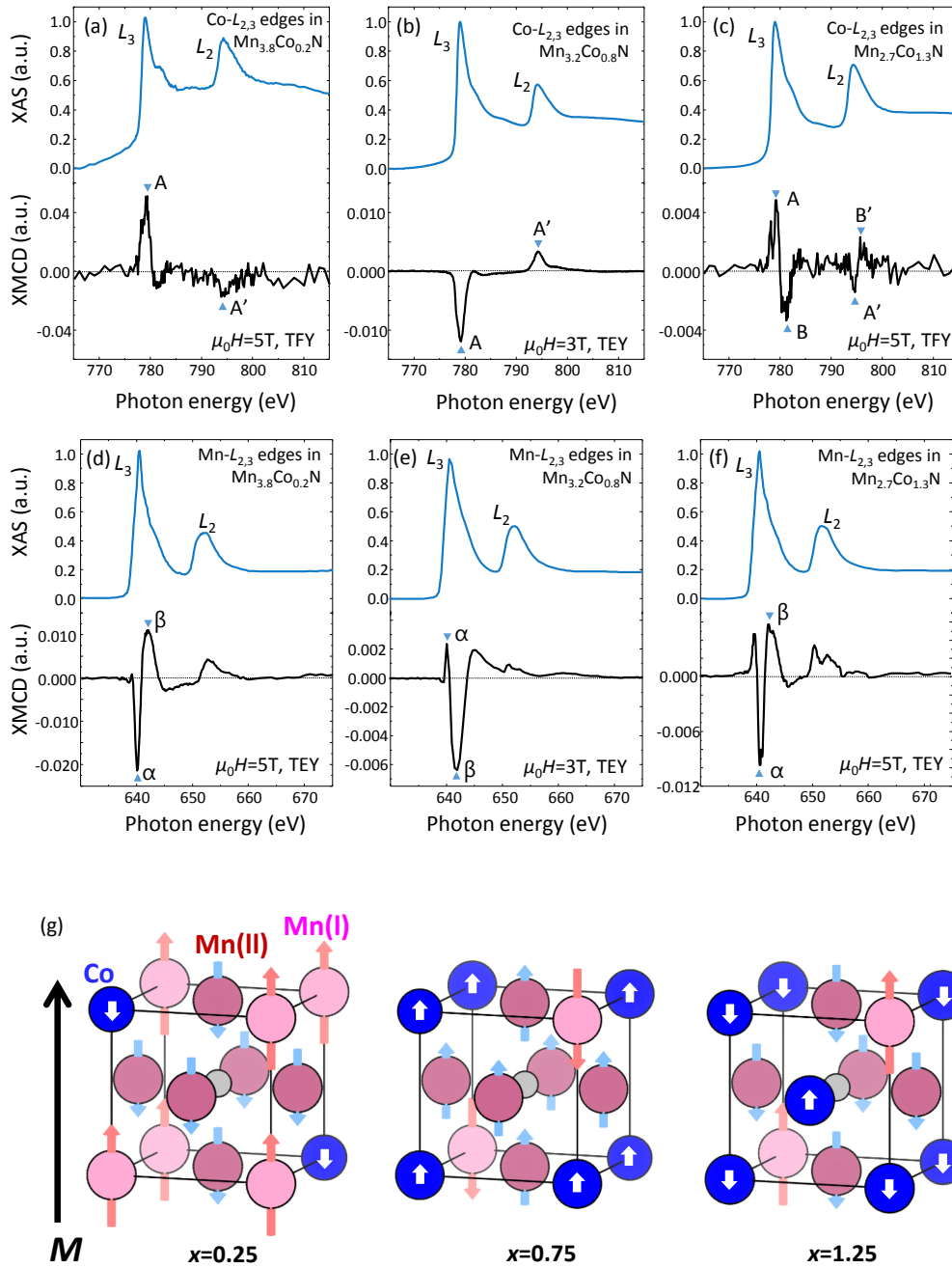
Fig. 11. (Color online) XAS (blue) and XMCD (black) spectra in (a, d) $Mn_{3.8}Co_{0.2}N$ films, (b, e) $Mn_{3.2}Co_{0.8}N$ films, and (c, f) $Mn_{2.7}Co_{1.3}N$ films at (a, b, c) Co-$L_{2,3}$ edges and (d, e, f) Mn-$L_{2,3}$ edges. Reproduced from Ref. 23 (©2020 American Physical Society). The sharp peak (α) and broad peak (β) in (d, e, f) originate mainly from Mn(I) and Mn(II), respectively. The reversal of the XMCD signals between (a) and (b) and between (d) and (e) means that the direction of magnetic moments of Mn and Co is reversed between them. In (c), the sign of the XMCD signal of Co(I) (A–A$'$) reverses again and another signal with the opposite sign (B–B$'$) of Co(II), appears, meaning that the magnetic moment of Co(II) is antiparallel to that of Co(I).

work,[22] Co atoms preferentially occupied I sites, Co(I) in $Mn_{4-x}Co_xN$ at $x = 0.8$, and the magnetic moment of Co(I) are aligned antiparallel to that of Mn(I). Thus, we can state that the Co atoms are supposed to be positioned at I sites when $x = 0.2$. The signs of the XMCD signals of Mn and Co reversed between $x = 0.2$ in Figs. 11(a), 11(b) and 0.8 in Figs. 11(d), 11(e), respectively, meaning that all the magnetic moments of Mn(I), Mn(II), and Co(I) reverse between these two compositions. We thereby conclude that the MC occurs in the range of $0.2 < x < 0.8$. At present, we do not have sufficient data to discuss the reason why the sign reversal was not observed in ρ_{AHE} between $x = 0.2$ and 0.8 in Fig. 10. Thus, further studies are mandatory on this issue.

The XMCD spectrum of Co at $x = 1.3$ in Fig. 11(c) is more complex than those of the other two compositions. This spectrum can be viewed as an overlap of two sets of components with opposite signs (A–A$'$ and B–B$'$). Notably, the sign of the peak A (A$'$) at $x = 1.3$ is opposite to that at $x = 0.8$. This result means that the magnetic moments of Co(I) atoms are reversed between these two compositions. Since the Co composition x is 1.3, which is higher than 1, some of the Co atoms are supposed to be positioned at II sites, Co(II). The peak position of B (B$'$) was slightly shifted from that of A (A$'$) to higher energies, similar to peaks α and β in Figs. 11(d) and 11(e). Thus, we recognize peaks B and B$'$ in Fig. 11(c) to originate from Co(II) atoms with their

magnetic moments aligned antiparallel to those of Co(I). We can therefore state that all the magnetic moments of Mn and Co atoms reverse between $x = 0.8$ and 1.3, indicating that MC occurs in the range of $0.8 < x < 1.3$. This is consistent with the sign reversal of ρ_{AHE} between $x = 1.1$ and 1.3 in Fig. 10. Based on the above discussions, we present simplified schematic illustrations of the magnetic structures in $Mn_{4-x}Co_xN$ in Fig. 11(g). We used $Mn_{4-x}Co_xN$ films at $x = 0.2$, 0.8, and 1.3 in this work; however, the Co compositions are 0.25, 0.75, and 1.25 in Fig. 11(g) to simplify the representation. Please note that we do not mean to exclude the possibility that all I sites are occupied with Co atoms when $x = 1.3$. Our findings show that the MC presumably occurs both between $x = 0.2$ and 0.8, and between $x = 0.8$ and 1.3. Observations of a MC at two low temperatures have already been reported[82] and have been studied theoretically.[83] However, to our knowledge there has been no report thus far of the existence of two MC compositions at RT just by doping.

5. Future Prospects of Mn₄N-based Ferrimagnets

At the vicinity of the MC in $Mn_{4-x}Ni_xN$ and $Mn_{4-x}Co_xN$, much faster v_{DW} than those obtained in Mn_4N can be achieved at RT,[80] as the efficiency of STT in these systems is primarily due to the low magnetization. The combination of SOTs to STTs in these layers, for instance by adding a neighboring spin Hall effect layer, might be beneficial for inducing DW motion and magnetization switching. To develop spintronics applications, it would also be worthwhile to check if the relatively high spin polarization of Mn₄N-based ferrimagnets could be used to obtain significant Tunnel Magnetoresistance ratios. Also, the double MC at RT found in $Mn_{4-x}Co_xN$ is very attractive from the viewpoint of applications. This is because the observed double MC mechanism might constitute a route to make the M_S small within a relatively wide range of Co concentrations, providing that one can find compensation concentrations close enough to each other. This is important because several magnetic quantities such as v_{DW} are quite sensitive to the composition change at the vicinity of the MC. For this reason, slight concentration variations may induce undesirable results. From the fundamental viewpoint, it would be interesting to compare the magnetic and spintronic properties such as SOT, STT, AHE, and polarization at the vicinity of the two MC concentrations. We suppose that double MC may occur also in $Mn_{4-x}Ni_xN$ at RT, when Ni atoms start to occupy the face-centered sites with their magnetic moments aligned with Mn(I) atoms when $x > 0.5$. In this context, double MCs are likely to occur in other Mn₄N-based ferrimagnets. As shown in Fig. 5(c), the DW mobility is quite high in Mn₄N, compared to those achieved using SOTs. However, the threshold current density, j_{th}, for DWs to start moving in Mn₄N, is relatively high, probably caused by a large damping constant α. It was measured to be around 0.1–0.2 at RT from the linewidth of microwave absorption spectra and the oscillation frequency of time-resolved MOKE signals.[84] This value is much greater than those reported on Fe₄N ($\alpha \sim 0.03$),[85] and higher by two orders of magnitude than those of MnGa alloys.[86] We are not sure why α is so large for Mn₄N at the moment. Thus extensive studies are mandatory to solve this issue. In any case, the results presented in this article

prove the versatility of doped Mn₄N thin films, and open up a rare-earth free platform for ferrimagnetic spintronics.

An unexplored aspect is the use of heavy metals to induce DMI and to take benefit of the SOT altogether with the STT. Thin layers of the Mn₄N family can be covered by a heavy metal in order to induce DMI and generate a transfer of angular momentum, to enhance the current-induced domain wall motion. It would be interesting to find a material combination where the direction of motion of STT and SOT adds up. If the DMI could be large, it would also be possible to obtain small skyrmions in thin Mn₄N layers, taking advantage of the magnetic properties and of the thermal stability, in order to develop memory and logic devices.[87,88]

Finally, the large tuning of the coercivity observed under a gate application through the STO substrate (Ref. 16) is another route to tailor the magnetic state of Mn₄N. This is a very appealing way to achieve a very energy efficient control of its magnetic properties. Yet the origin of this modulation, which could be linked to strain, charge transfer or ionic migration, has to be elucidated.

6. Conclusion

In this article, we review the potential of rare-earth free Mn₄N for spintronics, from the fundamental properties of Mn₄N such as the excellent epitaxial growth on STO(001) substrates, the AHE loops, and the domain structures observed by MOKE, to the latest results on CIDWM in Mn₄N-based microstrips, in which v_{DW} reaches $900\,\mathrm{m\,s^{-1}}$ in Mn₄N and $3,000\,\mathrm{m\,s^{-1}}$ in $Mn_{4-x}Ni_xN$ ($x = 0.15$). Mn₄N has a perpendicular magnetization, due to a high magnetic anisotropy constant of $\sim 10^5\,\mathrm{J\,m^{-3}}$, a small spontaneous magnetization of $\sim 100\,\mathrm{kA\,m^{-1}}$, and a large spin polarization as inferred from the large DW velocity. One of the striking features of this material is that magnetic compensation occurs at RT just by tuning its constituent element by doping. The sign reversal of the XMCD signals was observed in $Mn_{4-x}Ni_xN$ and $Mn_{4-x}Co_xN$ epitaxial films between below and above the MC compositions. The two different MC compensations appearing in $Mn_{4-x}Co_xN$ should also exist Mn₄N-based ferrimagnets. To further develop applications based on STTs and/or SOTs, several material properties have to be studied in more details, such as the spin current polarization and the damping parameter. Also, using and enhancing spin–orbit effects such as the SOTs or the DMI will require depositing ultrathin films of Mn₄N-based ferrimagnets, with a very high quality. These material developments could help confirming the potential of Mn₄N beyond DW manipulation by pure STT, from SOTs[14,89] to skyrmions[7,90] or THz switching.[91,92] We therefore hope that many researchers will be interested in using this material.

1) B. Dieny, I. L. Prejbeanu, K. Garello, P. Gambardella, P. Freitas, R. Lehndorff, W. Raberg, U. Ebels, S. O. Demokritov, J. Akerman, A. Deac, P. Pirro, C. Adelmann, A. Anane, A. V. Chumak, A. Hirohata, S. Mangin, S. O. Valenzuela, M. Cengiz Onbaşlı, M. d'Aquino, G. Prenat, G. Finocchio, L. Lopez-Diaz, R. Chantrell, O. Chubykalo-Fesenko, and P. Bortolotti, Nat. Electron. **3**, 446 (2020).
2) C. D. Stanciu, A. V. Kimel, F. Hansteen, A. Tsukamoto, A. Itoh, A. Kirilyuk, and Th. Rasing, Phys. Rev. B **73**, 220402(R) (2006).
3) C. D. Stanciu, A. Tsukamoto, A. V. Kimel, F. Hansteen, A. Kirilyuk, A. Itoh, and Th. Rasing, Phys. Rev. Lett. **99**, 217204 (2007).
4) S. Fukami, T. Suzuki, Y. Nakatani, N. Ishiwata, M. Yamanouchi, S. Ikeda, N. Kasai, and H. Ohno, Appl. Phys. Lett. **98**, 082504 (2011).
5) K.-J. Kim, S. K. Won, Y. Hirata, S.-H. Oh, T. Tono, D.-H. Kim, T. Okuno, W. S. Ham, S. Kim, G. Go, Y. Tserkovnyak, A. Tsukamoto, T. Moriyama, K.-J. Lee, and T. Ono, Nat. Mater. **16**, 1187 (2017).
6) Y. Hirata, D.-H. Kim, T. Okuno, T. Nishimura, D.-Y. Kim, Y. Futakawa, H. Yoshikawa, A. Tsukamoto, K.-J. Kim, S.-B. Choe, and T. Ono, Phys. Rev. B **97**, 220403(R) (2018).
7) L. Caretta, M. Mann, F. Buttner, K. Ueda, B. Pfau, C. M. Gunther, P. Hessing, A. Churikova, C. Klose, M. Schneider, D. Engel, C. Marcus, D. Bono, K. Bagschik, S. Eisebitt, and G. S. D. Beach, Nat. Nanotechnol. **13**, 1154 (2018).
8) S. A. Siddiqui, J. Han, J. T. Finley, C. A. Ross, and L. Liu, Phys. Rev. Lett. **121**, 057701 (2018).
9) S.-H. Oh, S. K. Kim, D.-K. Lee, G. Go, K.-J. Kim, T. Ono, Y. Tserkovnyak, and K.-J. Lee, Phys. Rev. B **96**, 100407(R) (2017).
10) R. Bläsing, T. Ma, S.-H. Yang, C. Garg, F. K. Dejene, A. T. N'Diaye, G. Chen, K. Liu, and S. S. P. Parkin, Nat. Commun. **9**, 4984 (2018).
11) S.-H. Yang, K.-S. Ryu, and S. Parkin, Nat. Nanotechnol. **10**, 221 (2015).
12) M. Binder, A. Weber, O. Mosendz, G. Woltersdorf, M. Izquierdo, I. Neudecker, J. R. Dahn, T. D. Hatchard, J.-U. Thiele, C. H. Back, and M. R. Scheinfein, Phys. Rev. B **74**, 134404 (2006).
13) T. Okuno, K.-J. Kim, T. Tono, S. Kim, T. Moriyama, H. Yoshikawa, A. Tsukamoto, and T. Ono, Appl. Phys. Express **9**, 073001 (2016).
14) K. Cai, Z. Zhu, J. M. Lee, R. Mishra, L. Ren, S. D. Pollard, P. He, G. Liang, K. L. Teo, and H. Yang, Nat. Electron. **3**, 37 (2020).
15) J. Yu, X. Qiu, Y. Wu, J. Yoon, P. Deorani, J. M. Besbas, A. Manchon, and H. Yang, Sci. Rep. **6**, 32629 (2016).
16) T. Gushi, M. J. Klug, J. P. Garcia, S. Ghosh, J.-P. Attané, H. Okuno, O. Fruchart, J. Vogel, T. Suemasu, S. Pizzini, and L. Vila, Nano Lett. **19**, 8716 (2019).
17) Z. Duan, A. Smith, L. Yang, B. Youngblood, J. Lindner, V. E. Demidov, S. O. Demokritov, and I. N. Krivorotov, Nat. Commun. **5**, 5616 (2014).
18) J. Finley, C. H. Lee, P. Y. Huang, and L. Liu, Adv. Mater. **31**, 1805361 (2019).
19) R. Mishra, J. Yu, X. Qiu, M. Motapothula, T. Venkatesan, and H. Yang, Phys. Rev. Lett. **118**, 167201 (2017).
20) T. Komori, T. Gushi, A. Anzai, L. Vila, J.-P. Attané, S. Pizzini, J. Vogel, S. Isogami, K. Toko, and T. Suemasu, J. Appl. Phys. **125**, 213902 (2019).
21) T. Komori, T. Hirose, T. Gushi, K. Toko, T. Hanashima, L. Vila, J.-P. Attàne, K. Amemiya, and T. Suemasu, J. Appl. Phys. **127**, 043903 (2020).
22) K. Ito, Y. Yasutomi, S. Zhu, M. Murmamat, M. Tahara, K. Toko, R. Akiyama, Y. Takeda, Y. Saitoh, T. Oguchi, A. Kimura, and T. Suemasu, Phys. Rev. B **101**, 104401 (2020).
23) H. Mitarai, T. Komori, T. Hirose, K. Ito, S. Ghosh, S. Honda, K. Toko, L. Vila, J.-P. Attané, K. Amemiya, and T. Suemasu, Phys. Rev. Mater. **4**, 094401 (2020).
24) C. Li, Y. Yang, L. Lv, H. Huang, Z. Wang, and S. Yang, J. Alloys Compd. **457**, 57 (2008).
25) G. Shirane, W. J. Takei, and S. L. Ruby, Phys. Rev. **126**, 49 (1962).
26) S. Kokado, N. Fujima, K. Harigaya, H. Shimizu, and A. Sakuma, Phys. Rev. B **73**, 172410 (2006).
27) Y. Komasaki, M. Tsunoda, S. Isogami, and M. Takahashi, J. Appl. Phys. **105**, 07C928 (2009).
28) K. Ito, K. Harada, M. Ye, A. Kimura, Y. Takeda, Y. Saitoh, H. Akinaga, and T. Suemasu, Appl. Phys. Lett. **99**, 252501 (2011).
29) K. Ito, T. Sanai, S. Zhu, Y. Yasutomi, K. Toko, S. Honda, S. Ueda, Y. Takeda, Y. Saitoh, Y. Imai, A. Kimura, and T. Suemasu, Appl. Phys. Lett. **103**, 232403 (2013).
30) F. Takata, K. Ito, S. Higashikozono, T. Gushi, K. Toko, and T. Suemasu, J. Appl. Phys. **120**, 083907 (2016).
31) M. Meinert, J. Phys.: Condens. Matter **28**, 056006 (2016).
32) W. J. Takei, R. R. Heikes, and G. Shirane, Phys. Rev. **125**, 1893 (1962).
33) K. Ito, Y. Yasutomi, K. Kabara, T. Gushi, S. Higashikozono, K. Toko, M. Tsunoda, and T. Suemasu, AIP Adv. **6**, 056201 (2016).
34) S. Isogami, K. Masuda, and Y. Miura, Phys. Rev. Mater. **4**, 014406 (2020).
35) K. Kuriyama, S. Hosoya, and T. Suzuki, Phys. Rev. **130**, 898 (1963).
36) S. Nagakura and N. Otsuka, J. Phys. Soc. Jpn. **39**, 1047 (1975).
37) S. Matar, P. Mohn, G. Demazeau, and B. Siberchicot, J. Phys. France **49**, 1761 (1988).
38) G. W. Wiener and J. A. Berger, JOM **7** [2], 360 (1955).
39) K. M. Ching, W. D. Chang, T. S. Chin, J. G. Duh, and H. C. Ku, J. Appl. Phys. **76**, 6582 (1994).
40) K. M. Ching, W. D. Chang, and T. S. Chin, J. Alloys Compd. **222**, 184 (1995).
41) M. Tsunoda and K. Kabara, presented at International Conference of the Asian Union of Magnetics Societies (ICAUMS), 2012, 2pPS-47.
42) Y. Yasutomi, K. Ito, T. Sanai, K. Toko, and T. Suemasu, J. Appl. Phys. **115**, 17A935 (2014).
43) X. Shen, A. Chikamatsu, K. Shigematsu, Y. Hirose, T. Fukumura, and T. Hasegawa, Appl. Phys. Lett. **105**, 072410 (2014).
44) K. Kabara and M. Tsunoda, J. Appl. Phys. **117**, 17B512 (2015).
45) T. Hirose, T. Komori, T. Gushi, K. Toko, and T. Suemasu, J. Cryst. Growth **535**, 125566 (2020).
46) T. Hirose, T. Komori, T. Gushi, A. Anzai, K. Toko, and T. Suemasu, AIP Adv. **10**, 025117 (2020).
47) A. Anzai, F. Takata, T. Gushi, K. Toko, and T. Suemasu, J. Cryst. Growth **489**, 20 (2018).
48) T. Komori, A. Anzai, T. Gushi, K. Toko, and T. Suemasu, J. Cryst. Growth **507**, 163 (2019).
49) S. Emori and G. S. D. Beach, Appl. Phys. Lett. **98**, 132508 (2011).
50) C. Burrowes, A. P. Mihai, D. Ravelosona, J.-V. Kim, C. Chappert, L. Vila, A. Marty, Y. Samson, F. Garcia-Sanchez, L. D. Buda-Prejbeanu, I. Tudosa, E. E. Fullerton, and J.-P. Attàne, Nat. Phys. **6**, 17 (2010).
51) A. Thiaville, J. M. García, and J. Miltat, J. Magn. Magn. Mater. **242–245**, 1061 (2002).
52) A. Mougin, M. Cormier, J. P. Adam, P. J. Metaxas, and J. Ferré, Europhys. Lett. **78**, 57007 (2007).
53) F. Parveen, Z. He, S. Angizi, and D. Fan, IEEE Computer Society Annual Symposium on VLSI (ISVLSI), 2017, p. 152.
54) S. Fukami and H. Ohno, Jpn. J. Appl. Phys. **56**, 0802A1 (2017).
55) M. Kawasaki, K. Takahashi, T. Maeda, R. Tsuchiya, M. Shinohara, O. Ishiyama, T. Yonezawa, M. Yoshimoto, and H. Koinume, Science **266**, 1540 (1994).
56) A. P. Mihai, J. P. Attané, A. Marty, P. Warin, and Y. Samson, Phys. Rev. B **77**, 060401(R) (2008).
57) V. D. Nguyen, L. Vila, P. Laczkowski, A. Marty, T. Faivre, and J. P. Attané, Phys. Rev. Lett. **107**, 136605 (2011).
58) T. Gushi, L. Vila, O. Fruchart, A. Marty, S. Pizzini, J. Vogel, F. Takata, A. Anzai, K. Toko, T. Suemasu, and J.-P. Attàne, Jpn. J. Appl. Phys. **57**, 120310 (2018).
59) H. Ohno, A. Shen, F. Matsukura, A. Oiwa, A. Endo, S. Katsumoto, and Y. Iye, Appl. Phys. Lett. **69**, 363 (1996).
60) V. D. Nguyen, L. Vila, P. Laczkowski, A. Marty, T. Faivre, and J.-P. Attané, Phys. Rev. Lett. **107**, 136605 (2011).
61) M. Meng, S. X. Wu, L. Z. Ren, W. Q. Zhou, Y. J. Wang, G. L. Wang, and S. W. Li, Appl. Phys. Lett. **106**, 032407 (2015).
62) K. Kabara, M. Tsunoda, and S. Kokado, AIP Adv. **7**, 056416 (2017).
63) K. Ito, N. Rougemaille, S. Pizzini, S. Honda, N. Ota, T. Suemasu, and O. Fruchart, J. Appl. Phys. **121**, 243904 (2017).
64) V. Gehanno, Y. Samson, A. Marty, B. Gilles, and A. Chamberod, J. Magn. Magn. Mater. **172**, 26 (1997).
65) J. P. Attané, Y. Samson, A. Marty, J. C. Toussaint, G. Dubois, A. Mougin, and J. P. Jamet, Phys. Rev. Lett. **93**, 257203 (2004).
66) M. Yamanouchi, A. Jander, P. Dhagat, S. Ikeda, F. Matsukura, and H. Ohno, IEEE Magn. Lett. **2**, 3000304 (2011).
67) F. Ando, H. Kakizakai, T. Koyama, K. Yamada, M. Kawaguchi, S. Kim, K.-J. Kim, T. Moriyama, D. Chiba, and T. Ono, Appl. Phys. Lett. **109**, 022401 (2016).
68) S. Emori, U. Bauer, S.-M. Ahn, E. Martinez, and G. S. D. Beach, Nat.

Mater. **12**, 611 (2013).

69) K.-S. Ryu, L. Thomas, S.-H. Yang, and S. Parkin, Nat. Nanotechnol. **8**, 527 (2013).

70) I. M. Miron, T. Moore, H. Szambolics, L. D. Buda-Prejbeanu, S. Auffret, B. Rodmacq, S. Pizzini, J. Vogel, M. Bonfim, A. Schuhl, and G. Gaudin, Nat. Mater. **10**, 419 (2011).

71) A. Thiaville, S. Rohart, É. Jué, V. Cros, and A. Fert, Europhys. Lett. **100**, 57002 (2012).

72) L. Caretta, M. Mann, F. Büttner, K. Ueda, B. Pfau, C. M. Günther, P. Hessing, A. Churikova, C. Klose, M. Schneider, D. Engel, C. Marcus, D. Bono, K. Bagschik, S. Eisebitt, and G. S. D. Beach, Nat. Nanotechnol. **13**, 1154 (2018).

73) C. O. Avci, E. Rosenberg, L. Caretta, F. Büttner, M. Mann, C. Marcus, D. Bono, C. A. Ross, and G. S. D. Beach, Nat. Nanotechnol. **14**, 561 (2019).

74) M. Mekata, J. Phys. Soc. Jpn. **17**, 796 (1962).

75) F. Takata, K. Ito, Y. Takeda, Y. Saitoh, K. Takanashi, A. Kimura, and T. Suemasu, Phys. Rev. Mater. **2**, 024407 (2018).

76) K. Ito, K. Toko, Y. Takeda, Y. Saitoh, T. Oguchi, T. Suemasu, and A. Kimura, J. Appl. Phys. **117**, 193906 (2015).

77) K. Ito, T. Sanai, Y. Yasutomi, S. Zhu, K. Toko, Y. Takeda, Y. Saitoh, A. Kimura, and T. Suemasu, J. Appl. Phys. **115**, 11C712 (2014).

78) E. Goering, S. Gold, and G. Schütz, J. Synchrotron Radiat. **8**, 422 (2001).

79) H. Maruyama and N. Nakamura, J. Electron Spectrosc. Relat. Phenom. **136**, 135 (2004).

80) S. Ghosh, T. Komori, A. Hallal, J. Pena Garcia, T. Gushi, T. Hirose, H. Mitarai, H. Okuno, J. Vogel, M. Chshiev, J. P. Attane, L. Vila, T.

81) Suemasu, and S. Pizzini, Nano Lett. **21**, 2580 (2021).

81) J. Stöhr and H. König, Phys. Rev. Lett. **75**, 3748 (1995).

82) S. Ohkoshi, T. Hozumi, M. Utsunomiya, M. Abe, and K. Hashimoto, Physica B **329–333**, 691 (2003).

83) Y. F. Zhang and S. L. Yan, Solid State Commun. **146**, 478 (2008).

84) S. Isogami, A. Anzai, T. Gushi, T. Komori, Y. K. Takahashi, and T. Suemasu, JSAP Spring Meeting, 2019, 10a-M101-7.

85) S. Isogami, M. Tsunoda, M. Oogane, A. Sakuma, and M. Takahashi, J. Magn. Soc. Jpn. **38**, 162 (2014).

86) S. Mizukami, F. Wu, A. Sakuma, J. Walowski, D. Watanabe, T. Kubota, X. Zhang, H. Naganuma, M. Oogane, and Y. Ando, Phys. Rev. Lett. **106**, 117201 (2011).

87) G. Yu, P. Upadhyaya, Q. Shao, H. Wu, G. Yin, X. Li, C. He, W. Jiang, X. Han, P. K. Amiri, and K. L. Wang, Nano Lett. **17**, 261 (2017).

88) W. Zhou, C. T. Ma, T. Q. Hartnett, P. V. Balachandran, and S. J. Poon, arXiv:2012.10493.

89) K. Ueda, M. Mann, P. W. P. de Brouwer, D. Bono, and G. S. D. Beach, Phys. Rev. B **96**, 064410 (2017).

90) Y. Hirata, D. H. Kim, S. K. Kim, D. K. Lee, S. H. Oh, T. Nishimura, T. Okuno, Y. Futakawa, H. Yoshikawa, A. Tsukamoot, Y. Tserkovnyak, Y. Shiota, T. Moriyama, S. B. Choe, K. J. Lee, and T. Ono, Nat. Nanotechnol. **14**, 232 (2019).

91) S. Mangin, M. Gottwald, C.-H. Lambert, D. Steil, V. Uhlíř, L. Pang, M. Hehn, S. Alebrand, M. Cinchetti, G. Malinowski, Y. Fainman, M. Aeschlimann, and E. E. Fullerton, Nat. Mater. **13**, 286 (2014).

92) S. Wienholdt, D. Hinzke, and U. Nowak, Phys. Rev. Lett. **108**, 247207 (2012).